PAPER

Check for updates

Nano-modified screen-printed electrode-based electrochemical immunosensors for oral cancer biomarker detection in undiluted human serum and saliva samples†

Payal Gulati,[a] Avinash Kumar Singh, [iD][a] Amit K. Yadav, [iD][a] Kiran Pasbola,[b] Prerna Pandey,[b] Rinu Sharma,[b] Alok Thakar[c] and Pratima R. Solanki [iD] *[a]

This proposed work reports the development of in-house made conductive ink-based screen-printed electrodes (SPEs) for label-free detection of oral cancer biomarkers. Carbon ink synthesis includes graphite powder, gum arabic, and water. The selectivity test of the fabricated SPE involves immobilizing antibodies specific to biomarkers and challenges with redox-active interference, other serum molecules, and non-target biomarkers. Three different biomarkers, cytokeratin-19 fragment (CYFRA 21-1), interleukin 8 (IL-8), and tumor protein p53 (TP-53), act as target entities for the detection of oral cancer in patients' samples (serum, $N = 28$, and saliva, $N = 16$) at an early stage. The standard technique enzyme-linked immunosorbent assay (ELISA) was employed to estimate the concentration of the biomarkers in serum and saliva samples. SPEs contain amine ($-NH_2$) functional groups involved in covalent bonding with the carboxyl ($-COOH$) groups of antibody molecules. These immunosensors exhibited remarkably lower detection limits of 829.5 pg mL^{-1}, 0.543 pg mL^{-1}, and 1.165 pg mL^{-1}, and excellent sensitivity of 0.935 μA mL pg^{-1} cm^{-1}, 0.039 μA mL pg^{-1} cm^{-1}, and 0.008 μA mL pg^{-1} cm^{-1} for CYFRA 21-1, IL-8, and TP-53 biomarkers, respectively. This sensing platform does not require any functionalization for biomolecule immobilization. Thus, it is a cost-effective, disposable, flexible, miniaturized, and sensitive strip to detect oral cancer biomarkers.

1. Introduction

Oral cancer (OC) is a type of carcinoma that starts as a growth in the mouth and affects different regions involving the lips, tongue, cheeks, the floor of the mouth, and pharynx (throat). The main cause that leads to the genesis of this cancer is the consumption of alcohol, chewing tobacco, smoking, betel quid, chronic inflammation, acid reflux, and contact with chemicals such as formaldehyde and asbestos or with any virulent species, *e.g.*, human papillomavirus.[1] Worldwide, it is rated the sixth most prevalent type of cancer and causes the second largest number of cancer cases. Around 77 000 new and 52 000 death cases are reported annually in India, which suggest $\frac{1}{4}$ of global incidences.[2] It is a life-threatening disease that requires biomarker availability for its timely detection and accurate prognosis. OC can be diagnosed with conventional techniques,

including laser-capture micro-dissection, visualization adjuncts, cytopathology, and biopsy. However, these techniques are laborious and costly, require trained personnel, are highly invasive, and are painful to patients.[3,4] Therefore, there is an urgent need to develop specific, non-invasive tools for OC diagnosis, which should be economical, accurate, and easier to handle.[3] Using a non-invasive detection tool is a promising strategy for detecting any disease in humans. Saliva is considered the best among all non-invasive fluids as it is easy to collect, store, and transport. In the case of OC, salivary biomarkers hold an additional advantage due to the direct contact of saliva with the cancer lesion, making saliva potentially more specific and sensitive. All the body fluids (blood, serum, breast fluid, and saliva) and cancer tissues have several metabolites, DNA, RNA, and proteins that provide insight for the detection of cellular alteration.[5–7] The saliva and serum biomarkers [cytokeratin-19 fragment (CYFRA 21-1), interleukin 8 (IL-8), and tumor protein p53 (TP-53)] have particular clinical significance in the detection of OC. The most common form of OC, Oral Squamous Cell Carcinoma (OSCC), causes impairment in oral epithelial cells due to the accumulation of genome alteration in the cells. IL-8 is essential in the angiogenesis and chemotaxis of granulocytes and macrophages. IL-8 is an

[a]Nano-Bio Laboratory, Special Centre for Nanoscience, Jawaharlal Nehru University, New Delhi-110067, India. E-mail: partima@mail.jnu.ac.in; pratimarsolanki@gmail.com

[b]University School of Biotechnology, Guru Gobind Singh Indraprastha University, India

[c]All India Institute of Medical Sciences, Ansari Nagar, New Delhi, 110029, India

indicator of OSCC's stroma cell. It is an indicator of the transformation of pre-cancerous lesions to oral cancer. CYFRA 21-1 studies telomerase activity in tumor cells. CYFRA 21-1 also maintains the telomere length during the replication of chromosomes. A report presented by Sawant et al.[8] mentioned the sensitivity and specificity of the CYFRA 21-1 biomarker as 84% and 93%, respectively, in oropharyngeal cancer patients.[9–12] TP-53 is a genomic biomarker for OSCC detection. The loss of heterozygosity (LOH) in chromosomes (9p, 3q, 13q, and 17p) is an early marker in oral carcinoma genesis. Liao et al. noticed a TP-53 gene mutation on the 17p chromosome in the DNA of OSCC patients in their saliva samples, suggesting that TP-53 can be a potential biomarker for OSCC detection. When DNA damage occurs, the TP-53 gene arrests the cell cycle and initiates apoptosis.[13,14] The clinical significance of these biomarkers indicates cancer's physiology and pathological conditions at any stage.

Moreover, a few research groups have been working on detecting OC with the help of various biomarkers by using different immunosensors based on electrochemical detection methods. Specific reports present IL-8 as a potential biomarker. Wan et al. (2011) deposited MWCNTs onto a disposable screen-printed carbon electrode (SPCE) to make an ultrasensitive immunosensor.[15] Verma et al. utilized a composite of gold nanoparticles/reduced graphene oxide (AuNPs–rGO). They found a detection limit of 72.73 ± 0.18 pg mL^{-1} (ref. 16) and later on, with a zinc oxide–reduced graphene oxide (ZnO–rGO) nanocomposite the detection limit enhanced to 51.53 ± 0.43 pg mL^{-1} (ref. 17). Sharma et al. fabricated a biosensor for IL-8 detection using capture protein, which acts as a synthetic non-antibody made from a cystatin scaffold. It demonstrated an enhanced LOD of up to 90 fg mL^{-1} and a K_D value of 35 ± 10 nM, representing a considerable affinity for human IL-8.[18]

In addition to IL-8, other biomarkers were also utilized as OC biomarkers. Therefore, few reports represent the use of CYFRA-21-1 as a biomarker. Tiwari et al. (2016) utilized L-cysteine-capped lanthanum hydroxide nanostructures for non-invasive CYFRA 21-1 detection and reported 0.001 ng mL^{-1}.[19] Wang et al. (2017) used a novel nanocomposite of multifunctional poly(thionine)–Au and found a wide detection limit of 4.6 fg mL^{-1}.[20] Pachauri et al. (2018) reported cerium oxide nano-cubes (ncCeO$_2$) with a reduced graphene oxide (RGO)-nanocomposite and found a detection limit of 0.625 pg mL^{-1}.[21] One newly reported novel biomarker, TP-53, is also targeted for OC detection. Wilson et al. (2005) reported a novel optical biosensor detecting TP-53 mutations.[22] A comparative table of reported and the present immunosensors is given in Table 1.

Reported immunosensors in the literature have used costly substrates such as indium tin oxide (ITO),[23,24] silicon wafers, fluorine tine oxide (FTO), and glassy carbon electrodes (GCEs) for sensor fabrication. These electrodes are sensitive, but their fabrication cost is high, and cutting them into the desired size is a laborious procedure. Moreover, these electrodes require additional cleaning procedures to remove impurities. Therefore, the preferred choice is laboratory-made carbon ink-based screen-printed electrodes (SPEs). SPEs consist of a three-electrode system composed of working, auxiliary, and

Table 1 Comparison table of the current immunosensors with previously reported immunosensor studies

S. no.	Electrode	Biomarkers	Technique	Detection range	Sensitivity	LOD	Ref.
1	Screen-printed carbon electrode (SPCE)	IL-8	Electrochemical	8–1000 pg mL^{-1}	—	8 pg mL^{-1}	15
2	Anti-IL8/AuNPs–rGO/ITO	IL-8	Electrochemical	500 fg mL^{-1} to 4 ng mL^{-1}	—	72.73 ± 0.18 pg mL^{-1}	16
3	Anti-IL8/ZnO–rGO/ITO	IL-8	Electrochemical	100 fg mL^{-1} to 5 ng mL^{-1}	2.46 ± 0.82 μA mL ng^{-1}	51.53 ± 0.43 pg mL^{-1}	17
4	SAM/gold electrode	IL-8	Electrochemical	900 fg mL^{-1} to 900 ng mL^{-1}	—	90 fg mL^{-1}	18
5	BSA/anti-CYFRA-21-1/Cys-La(OH)$_3$/ITO	CYFRA 21-1	Electrochemical	0.001–10.2 ng mL^{-1}	12.044 μA mL ng^{-1}	0.001 ng mL^{-1}	19
6	Anti-CYFRA21-1/poly(thionine)–Au nanocomposite modified GCE	CYFRA 21-1	Electrochemical	100 ng mL^{-1} to 10 fg mL^{-1}	—	4.6 fg mL^{-1}	20
7	BSA/anti-Cyfra-21-1/ncCeO$_2$–RGO/ITO	CYFRA 21-1	Electrochemical	0.625 pg mL^{-1} to 15 ng mL^{-1}	14.5 mA ng^{-1} mL cm^{-2}	0.625 pg mL^{-1}	21
8	Gold electrode	TP-53	Optical	—	—	—	22
9	**SPE**	**CYFRA 21-1**	**Electrochemical**	**0–20 ng mL^{-1}**	**0.935**	**829.5 pg mL^{-1}**	**Present work**
		IL-8		0–2000 pg mL^{-1}	0.039	0.542 pg mL^{-1}	
		TP-53		0–5000 pg mL^{-1}	0.008 μA mL pg^{-1} cm^{-1}	1.165 pg mL^{-1}	

reference electrodes on a single strip. The novelty of this electrode is cost-effective, disposable, miniaturized, sensitive, flexible, and bio-compatible for biomolecule detection. This electrode upgradation is possible for point-of-care (POC) device fabrication.

The primary technology platform nowadays incorporates POC devices with biosensors to form compact and portable medical systems capable of diagnosing on-site medical conditions. POCT offers certain merits, including rapid response, low cost, high durability, and high selectivity and sensitivity. In contrast to several traditional detection methods, POCT can rapidly and accurately detect disease with fewer patient samples for analysis. Moreover, it demands a smaller number of analysis tools. Furthermore, advancement in medical healthcare diagnostics and devices can be brought about by emerging technologies, including artificial intelligence (AI) and the Internet of Medical Things (IoMT).[25] The improvement provided by the IoMT and the Internet of Things (IoT) is the real-time monitoring of patients by doctors through remote detection and data collection systems.[26] The benefits of combining the IoT and wearable sensors include tracking patients' health and well-being, detecting health-related problems in elderly or differently abled people, and providing specific treatment plans.[27,28]

In this work, we report conductive ink synthesis using graphite powder and gum arabic and then printing on an appropriate substrate with the help of a screen-printing machine and stencil. Here, we developed three different immunosensors for the detection of CYFRA 21-1, IL-8, and TP-53 biomarkers, and these cover the entire physiological range (3.8 to 17.46 ± 1.46 ng mL^{-1}; 130 ± 250 to 750 ng mL^{-1}; 0.5 ± 0.23 to 1.03 ± 0.59 ng mL^{-1}, respectively) secreted in the body fluid of the standard and oral cancer patients. Electrochemical sensing was performed with respective antigens, and dilutions were prepared for all three biomarkers. The detection limit of all three immunosensors was calculated from the calibration plot (peak current *vs.* antigen concentration). Subsequently, patient serum ($N = 28$) and saliva ($N = 16$) samples were also tested for all three biomarkers using immunosensors, and concentrations were calculated from the standard technique ELISA.

2. Experimental procedure

2.1. Reagents required

Bovine serum albumin (BSA) and linker molecules such as *N*-hydroxysuccinimide (NHS) and *N*-ethyl-*N*′-(3-dimethyl aminopropyl) carbodiimide hydrochloride (EDC) were procured from Sigma-Aldrich. Other reagents such as sodium hydroxide (NaOH), acetone, ethanol, toluene, potassium ferrocyanide ([Fe(CN)$_6$]$^{4-}$), and potassium ferricyanide ([Fe(CN)$_6$]$^{3-}$) were purchased from Fischer Scientific. Monobasic sodium phosphate anhydrous (NaH$_2$PO$_4$) and di-basic sodium phosphate dihydrate (Na$_2$HPO$_4$), and certain other chemicals like potassium chloride, glucose, urea, uric acid, ascorbic acid, and NaCl were purchased from SRL Pvt Ltd, in India. Biomarkers such as CYFRA 21-1, IL-8, and TP-53, along with their respective antibodies, including anti-CYFRA 21-1, anti-IL-8 and anti-TP-53, were procured from My Biosource, USA and stored at -20 °C.

Phosphate buffer saline (PBS) was prepared (pH = 7.4) to reconstitute the antibodies and dilutions of all the proposed biomarkers. ELISA kits of CYFRA-21-1, IL-8, and TP-53 were purchased from CUSABIO, USA. PBS buffer was stored at 4 °C until further use. All the antibodies and antigen protein dilutions were prepared in PBS (pH = 7.4) using Millipore water of 18.25 MΩ cm^{-1}. A rough substrate (electro-coated waterproof silicon carbide rough paper) was purchased from a nearby electrical appliances shop. Graphite powder was procured from Alfa Aesar. PBS (0.2 M) containing 5 mM ([Fe(CN)$_6$]$^{3-/4-}$) buffer was used for the sensing study.

2.2. Preparation of graphite-based conductive ink

Graphite-based conductive ink comprises three fundamental elements: a carrier, a binder, and a functional material.[29] The functional material (graphite) promotes conductivity; carrier molecules (water) are involved in homogeneous mixture formation with a functional material. In contrast, gum arabic as a binder controls the mixture's viscosity and holds the elements together.[29] 30 mL ink preparation incorporates 6 g of gum arabic in 20 mL of boiling water (100 °C) under continuous stirring and the mixture is let to cool down to room temperature (RT), and then 19.2 g of graphite powder ($\sim$44 nm, particle size) is added in batches of 5 g under continuous agitation of the mixture. The obtained ink is black, homogeneous, and viscous.

2.3. Selection of substrates

Substrate optimization is necessary to ensure complete adhesion of carbon ink over the substrate surface. Three different substrates, such as ivory sheet, PET substrate, and rough paper, were chosen for contact angle measurement to study the hydrophobicity and hydrophilicity. The substrate's nature decides the ink's stability over its surface and allows the ink to take electrode shape without distortion. The electrochemical behavior of electrodes was also tested through the cyclic voltammetric (CV) technique to check the oxidation-reduction peak currents (Fig. S1[c–e]†).

2.4. Printing methodology

Printing utilizes a polyester mesh with 46 thread size and two different squeegees (black and green) of 48 cm in length for printing with medium pressure on the stencil screen and 400 mm s^{-1} printing speed. The substrate was electro-coated waterproof silicon carbide rough paper, grey. The print consists of three electrodes, working, counter, and reference electrodes. The printed electrodes were then cured at 80 °C in an oven for 15 minutes. Silver paste coating on the reference electrode generates a potential difference between the counter and reference electrodes.

2.5. Characterization techniques

The CV technique was performed using an Autolab, potentiostat/galvanostat electrochemical analyzer (EcoChemie, The Netherlands). Scanning electron microscopy (SEM) (JSM-IT 200) confirms the continuous connection between electrodes

and conducting paths. Fourier transform infrared spectroscopy (FT-IR) was used to verify the presence of functional groups over the conductive graphite-based SPEs and various modifications done over the working electrode. The FT-IR spectra were obtained in the 4000 to 400 cm^{-1} wavenumber range *via* the PerkinElmer Spectrum 1 configuration of the FT-IR spectrometer unit. The contact angle measurement was done using a drop-shape analyzer [KRUSS, Germany] to check the hydrophobicity/hydrophilicity of the substrate required for SPE fabrication. The screen printing of SPE requires a GRAFICA Flextronica machine.

2.6. Immunosensor fabrication

The sensing surface (*i.e.*, working electrode) of SPEs contains several functional groups, such as carboxylic, hydroxyls, and amines, which actively participate in bond formation. Therefore, this substrate does not require any sort of functionalization to generate active sites, and direct antibody immobilization is possible. This step requires immobilizing respective biomarker antibodies on the different electrodes for the preparation of three other immunosensors. Furthermore, 10 μg mL^{-1} concentration of anti-CYFRA 21-1; anti-IL-8 and anti-TP-53 antibodies were activated *via* mixing with coupling molecules, 0.1 M NHS and an activator agent, 0.4 M EDC [prepared in PBS (pH = 7.4)] in a ratio of 2 : 1 : 1 and incubating for 45 min before use. After that, the activated antibodies (5 μL) were immobilized over a working electrode involving 5 h incubation in

a humidified chamber maintained at 25 °C, followed by washing with 4 μL of PBS (pH = 7.4) to remove unbound antibody molecules. This step involves the formation of covalent amide bonds between the –COOH group of antibodies on the Fc fragment and the amine functional group over the working electrode. The reaction chemistry includes antibody –COOH group activation through EDC, generating unstable *O*-acylisourea ester, which tends to form a stable intermediate product (*i.e.*, amine-reactive NHS ester) upon reaction with NHS. This stable intermediated product readily reacts with the –NH$_2$ groups present over the working electrode.[30,31] Subsequently, the non-binding sites on the electrode surface were blocked with 1% BSA (4 μL) to avoid non-specific signals. BSA was immobilized on the electrode surface by incubating for 1.5 h in a humidified chamber, followed by washing with PBS (pH = 7.4).[32] These three different immunosensors, BSA/anti-CYFRA 21-1/SPE, BSA/anti-IL-8/SPE, and BSA/anti-TP-53/SPE, were utilized for the detection of CYFRA 21-1, IL-8 and TP-53 antigens, respectively. These synthesized immunosensors were stored at 4 °C until used for sensing. The general scheme involved in this immunosensor fabrication is illustrated in Scheme 1.

2.7. Preparation of analyte(s) dilutions

The stock concentration (75 μg mL^{-1}) of CYFRA 21-1 protein was diluted in PBS, pH = 7.4, to obtain various concentrations ranging from 0.1 ng mL^{-1} to 20 ng mL^{-1}. Similarly, the other two proteins, IL-8 and TP-53, were diluted from their respective
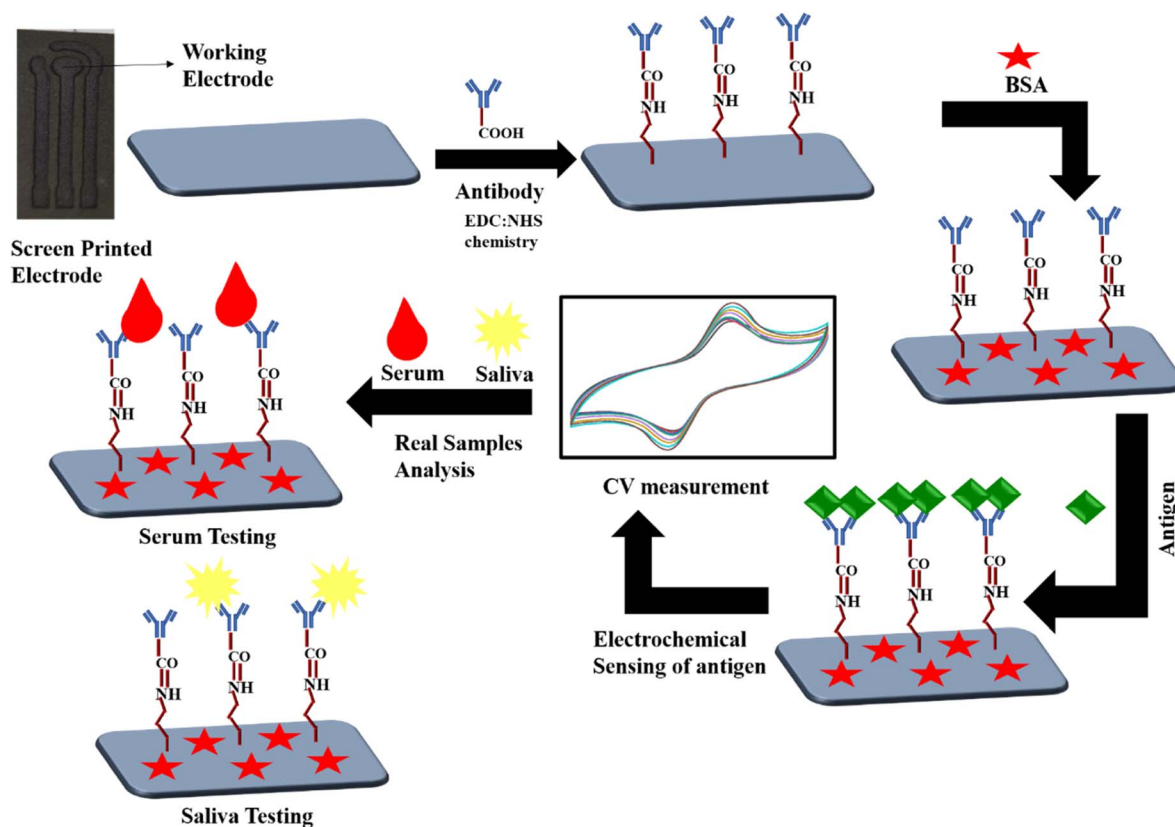
Scheme 1 Schematic of the SPE–based immunosensor through immobilization of antibodies, BSA, and antigens.

stock concentrations (100 μg mL^{-1} and 1 mg mL^{-1}) in a range from 100 pg mL^{-1} to 1000 pg mL^{-1} and from 1 pg mL^{-1} to 5000 pg mL^{-1}, respectively. The response of all the proposed immunosensors was studied *via* the CV measurement technique in 0.2 M PBS (pH 7.4) containing 5 mM [Fe(CN)$_6$]$^{3-/4-}$.

2.8. Patient sample collection and processing

The proposed biomarkers (CYFRA 21-1) were analyzed in patient serum and saliva samples to test the efficiency of the fabricated immunosensors. OC patient samples were collected from the All India Institute of Medical Sciences (AIIMS), New Delhi. The collected blood samples were allowed to stand in a vial for about 20 minutes, followed by centrifugation at 4 °C at 3000 rpm for 10 minutes, and the obtained supernatant contained serum. Aliquots of 100 μL were made and stored at −80 °C. The saliva samples were processed by centrifuging at 10 000 rpm for 10 min at 4 °C, and then collecting the supernatant and making 100 μL aliquots before storing at −80 °C. Saliva centrifugation is essential to remove insoluble materials such as cellular debris, bacteria, and aggregates of glycoproteins.[33,34]

2.9. Standardization of experimental conditions

The standardization of experimental conditions includes antibody concentration and buffer pH [Fig. S1(a and b)†], to fabricate the most efficient immunosensors. The pH has a strong influence on immunosensors. Therefore, the response of all three fabricated immunosensors (BSA/anti-CYFRA 21-1/SPE; BSA/anti-IL-8/SPE; BSA/anti-TP-53/SPE) was measured by studying the change in electrochemical response in both acidic and basic media. The results are given in the ESI in Section S1.1.† Furthermore, a CV study was done to perform substrate optimization with different substrates, including PET, ivory sheet, and sandpaper, shown in the ESI (Section S1) in Fig. S1(c–e).†

2.10. Live subject statement

All experiments were performed in compliance with the relevant laws and institutional guidelines of the All India Institute of Medical Sciences (AIIMS) and Jawaharlal Nehru University (JNU) Ethics Committee for patient sample collection that has approved the experiments. Patients too signed the consent form, confirming their participation at the time of blood and saliva sample collection.

3. Results and discussion

3.1. Contact angle measurement

To fabricate SPEs with high precision and quality, surface affinity is the main contributing factor. The hydrophilicity or hydrophobicity of the substrate decides the adhesive strength between the ink and substrate. Therefore, it is essential to measure the hydrophilicity or hydrophobicity of the substrate. The water contact angle (θ) on three different substrates was detected to explore the most suitable substrate for SPEs fabrication. The obtained θ values shown in Fig. 1(a–c) for the different substrates, including PET (polyethylene terephthalate), ivory sheet, and sandpaper (electro-coated waterproof, silicon carbide paper), were 68.4°, 110.15° and 124.05°, respectively. These results suggest sandpaper to be the most appropriate substrate due to its hydrophobicity. As gum arabic is a hydrophobic element in the mixture, it increases the adhesion of the ink to the hydrophobic surface, *i.e.*, rough paper.[10] Ink is water-based; therefore, it requires an appropriate hydrophobic substrate to prevent ink from peeling off.

3.2. Characterization of in-house screen-printed electrodes (SPEs)

The surface morphology of the bare SPEs was studied by scanning electron microscopy (SEM) [Fig. 2(a)]. Energy dispersive X-ray analysis (EDX) [Fig. 2(b)] was used to study the material composition. The micrograph shows a continuous conducting path throughout the electrode surface. In contrast, the EDX graph indicates the presence of carbon and oxygen, which verifies that the ink composition has a conductive carbon source. Fig. 2(c) shows the FT-IR spectrum of the bare SPE presenting two characteristic peaks of graphite at 2399 cm^{-1} and 3384 cm^{-1}, corresponding to CO_2 and C–OH, suggesting graphite's porous and hygroscopic nature.[35] Some other characteristic peaks of gum arabic observed at 3383 cm^{-1}, 2399 cm^{-1}, 1649 cm^{-1}, and from 900–1200 cm^{-1} represent O–H stretching (characteristic of glucosidic bond), C–H stretching, COO– symmetric stretching and fingerprint of carbohydrates, respectively.[36] The gum arabic comprises hydroxyls, carboxylic, and amine groups in its compound structure.

3.3. Spectroscopic and morphological study of the fabricated electrodes

FT-IR identifies the functional groups over the fabricated immunosensor [represented in Fig. 3(a)] and identifies which
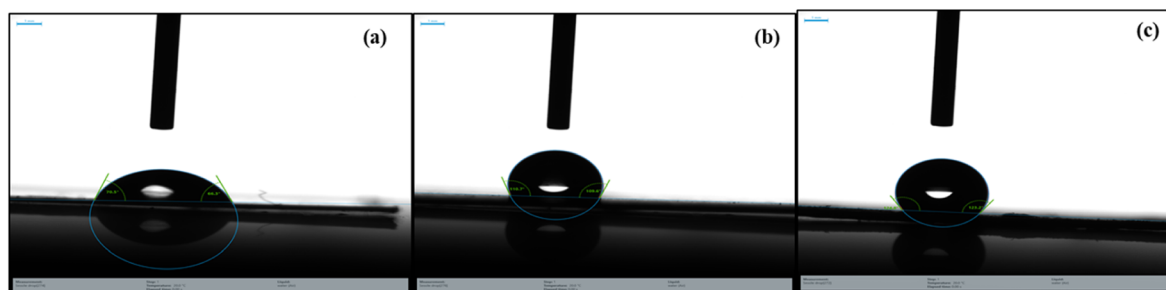

Fig. 1 Contact angle study before electrode printing: (a) bare PET substrate, (b) bare ivory sheet, and (c) bare sandpaper.
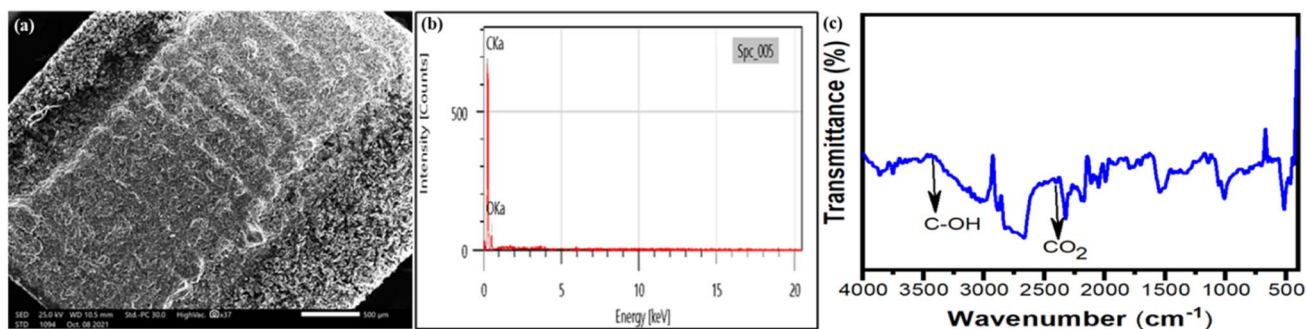
Fig. 2 Bare screen-printed electrodes study: (a) scanning electron micrograph; (b) energy dispersive X-ray spectrum; (c) Fourier transform infrared spectrum.

functional bonds of biomolecular species are involved in bond formation with the SPE surface. The characteristic peaks obtained after antibody and BSA immobilization are given in the chart in Fig. 3(b), confirming their attachment with the SPE.

Moreover, SEM images provide a visual narrative of the surface evolution of SPEs through various stages. In the case of bare-SPEs, SEM typically reveals a smooth and relatively pristine surface, characteristic of the base electrode material. Minute surface imperfections or minor defects may be visible, reflecting the intricacies of the fabrication process [Fig. 3(c)]. However, a discernible transformation occurs after the immobilization of antibodies on the electrode's surface. SEM images depict the emergence of irregular structures and clusters, representing the immobilized antibodies, as shown in Fig. 3(d). This may manifest as roughness or irregularities on the electrode's surface, denoting the successful attachment of antibodies.[37] Following the immobilization of BSA, SEM images portray yet another layer of structural change. BSA immobilization results in a comparatively smooth and continuous coating, distinct from the irregular clusters formed by the antibodies Fig. 3(e).[38]

3.4. Scan rate study

The effect of the scan rate on the oxidation/reduction peak current was measured from CV response. Scan rate studies of different electrodes, including the bare SPE, anti-CYFRA 21-1/ SPE, BSA/anti-CYFRA 21-1/SPE, anti-IL-8/SPE, BSA/anti-IL-8/
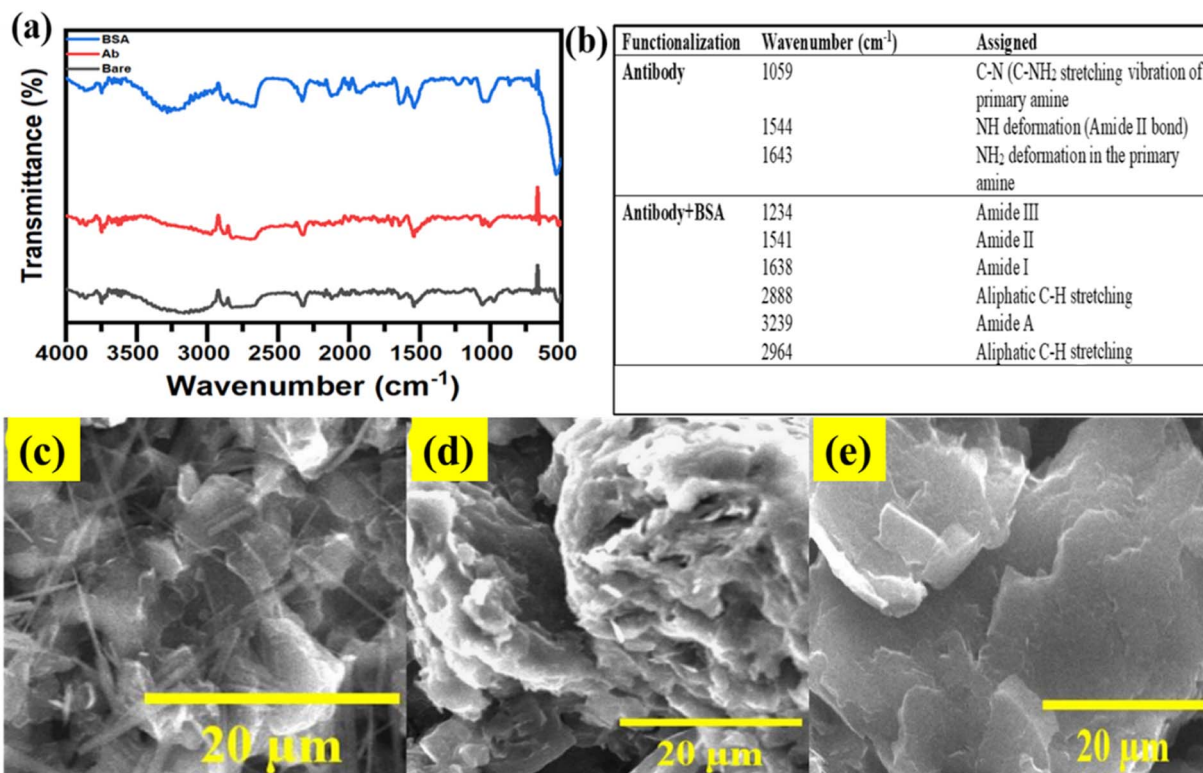

Fig. 3   (a) FTIR spectra of the bare SPE surface, after antibody and BSA immobilization on immune-electrodes; (b) chart representing assignments of peaks in the FTIR spectra after antibody and BSA treatment; SEM images of (c) bare SPEs; (d) after immobilization of antibodies (anti-CYFRA 21-1/SPE); and (e) BSA (BSA/anti-CYFRA 21-1/SPE).

SPE, anti-TP-53/SPE and BSA/anti-TP-53/SPE (Fig. S2 in the ESI†), analyze the electro-kinetics at the interface and electrolyte of the electrodes. The scan rate study was performed within the potential range from −0.8 V to +0.8 V and at various scan rates from 10 to 100 mV s^{-1}, shown in Fig. S2.† The inset of Fig. S2† shows that the redox anodic (I_{pa}) and cathodic (I_{pc}) peak current increased linearly with increasing scan rate and proportional to the square root of the scan rate ($v^{1/2}$), given in equations below from eqn (1) to (7). This increase in current suggests a diffusion-controlled electrochemical reaction at the electrode's surfaces.[39,40] The peak current ratio (I_{pa}/I_{pc}) at 50 mV s^{-1} for the immunoelectrodes such as the bare SPE, anti-CYFRA 21-1/SPE, BSA/anti-CYFRA 21-1/SPE, anti-IL-8/SPE, BSA/anti-IL-8/SPE, anti-TP-53/SPE and BSA/anti-TP-53/SPE was calculated to be 1.08, 1.04, 1.09, 1.07, 1.08, 1.06 and 1.07, respectively, representing a reversible electron transfer process. The obtained results suggest efficient electron transportation from electrolytes toward electrode surfaces.

$$I_{pc}(\text{bare SPE}) = 2.5483 \ \mu A \ (s \ mV^{-1})$$
$$\times (\text{scan rate } [mV \ s^{-1}]^{1/2} - 6.8719), R^2 = 0.984 \tag{1}$$

$$I_{pc}(\text{anti-CYFRA 21-1/SPE}) = -6.81 \ \mu A \ (s \ mV^{-1})$$
$$\times (\text{scan rate } [mV \ s^{-1}]^{1/2} + 2.701), R^2 = 0.983 \tag{2}$$

$$I_{pc}(\text{BSA/anti-CYFRA 21-1/SPE}) = -11.35 \ \mu A \ (s \ mV^{-1})$$
$$\times (\text{scan rate } [mV \ s^{-1}]^{1/2} + 3.15), R^2 = 0.982 \tag{3}$$

$$I_{pc}(\text{anti-IL-8/SPE}) = -14.83 \ \mu A \ (s \ mV^{-1})$$
$$\times (\text{scan rate } [mV \ s^{-1}]^{1/2} + 5.06), R^2 = 0.984 \tag{4}$$

$$I_{pc}(\text{BSA/anti-IL-8/SPE}) = -12.65 \ \mu A \ (s \ mV^{-1})$$
$$\times (\text{scan rate } [mV \ s^{-1}]^{1/2} + 5.28), R^2 = 0.987 \tag{5}$$

$$I_{pc}(\text{anti-TP-53/SPE}) = -11.07 \ \mu A \ (s \ mV^{-1})$$
$$\times (\text{scan rate } [mV \ s^{-1}]^{1/2} + 4.18), R^2 = 0.98 \tag{6}$$

$$I_{pc}(\text{BSA/anti-TP-53/SPE}) = -11.28 \ \mu A \ (s \ mV^{-1})$$
$$\times (\text{scan rate } [mV \ s^{-1}]^{1/2} + 4.41), R^2 = 0.972 \tag{7}$$

The calculation of all the other parameters (such as D_f, A_e, and I^*) is mentioned in the ESI in Table S1.†

3.5. Electrochemical response studies of the three immunosensors

The biological signals of the human body are electrochemical. Thus, electrochemical measurements of immunosensors to study the response of all three proposed immunosensors are preferable.[41] Electrochemistry was studied with an electrolyte containing redox species $[Fe(CN)_6]^{3-/4-}$ to study the redox behaviour of biological species within a wide potential window. These redox species promote electron transfer by enhancing an oxidation and reduction peak current. CV is an effective method for studying the step-wise changes performed over the electrode surface and calculating the sensor's detection limit.[48]

3.5.1 CYFRA 21-1 biomarker-based immunosensor response. Fig. 4(a) shows the successful step-wise modification

on the SPE surface with a change in anodic and cathodic peak current after anti-CYFRA21-1 Ab and BSA immobilization. The current was enhanced after both the immobilizations, *i.e.*, anti-CYFRA 21-1/SPE and BSA/anti-CYFRA 21-1/SPE compared to the bare SPE surface. The reason behind this lies in the structure of bulk graphite, composed of sp^2 hybridized graphene layers interacting with weak van der Waals forces and π–π interactions of the delocalized electron orbitals.[42] The weak *van der Waal* forces between 2D graphene layers allow the intercalation of biological species and ionic molecules across the edge planes, thus causing interlayer expansion, eventually leading to the rearrangement of graphene layers (Fig. 5).[43] Consequently, it produces defects inside the graphite structure, which enhances the current flow, *i.e.*, promotes electron transfer over the electrode surface (the details of the charge transfer mechanism are given in Section 5; Fig. 13).

Similarly, the current level increased when the immune-electrode was exposed to different concentrations of CYFRA 21-1 antigen ranging from 0.1 ng to 20 ng mL^{-1} [Fig. 4(b)].[44] Antigens are bulky, and when they form an immune complex with antibodies, they cause defect formation inside the graphite structure, promoting enhanced current flow over the electrode surface. Fig. 4(c) shows the calibration plot (peak current *vs.* CYFRA 21-1 antigen concentration) representing a linearity of 0.95. Moreover, the calculated limit of detection (LOD) and sensitivity values are 829.5 pg mL^{-1} and 0.935 μA mL pg^{-1} cm^{-1}, respectively.

The interferent study in the presence of various control species was analyzed to confirm the immunosensor specificity (BSA/anti-CYFRA 21-1/SPE). These control species include the analytes in human body fluids such as glucose, NaCl, ascorbic acid, uric acid, urea, oxalic acid, and other biomarkers such as SP-17, TP-53, and IL-8. Fig. 4(d) represents the change in anodic peak current upon adding other interferent species in the presence of the CYFRA 21-1 biomarker. A significant decrease was seen after immune-complex formation between anti-CYFRA 21-1 and CYFRA 21-1 antigens compared to other interferents, depicting the specificity of the biosensor.

The Hanes–Woolf plot estimates the binding affinity between the antigen and antibody on the surface of the fabricated immune-electrode. The affinity test for the biomarker on the surface of the immunoelectrode helps to assess the sensor's efficiency. The Hanes–Woolf plot represents antigen concentration *vs.* antigen conc./change in current that gives the value of the dissociation constant (K_d).[45] K_d value can be calculated by dividing the intercept with a slope of the Hanes–Woolf plot. Fig. 3(e) shows the Hanes–Woolf plot for the immune-electrode BSA/anti-CYFRA 21-1/SPE to test the binding affinity between CYFRA 21-1 and anti-CYFRA 21-1 and calculated $K_d = 0.318$ ng mL^{-1}.

Fig. 3(f and g) shows the change in anodic peak current in the bar graph of oral cancer patients' serum and saliva samples for the BSA/anti-CYFRA 21-1/SPE immunoelectrodes, respectively. The anodic peak current value was found to be much higher in the case of saliva samples in comparison to serum samples (Tables 2 and 3), as saliva is in direct contact with the lesion. Therefore, saliva contains a higher concentration of OC biomarkers, confirmed by the conventional method ELISA. In
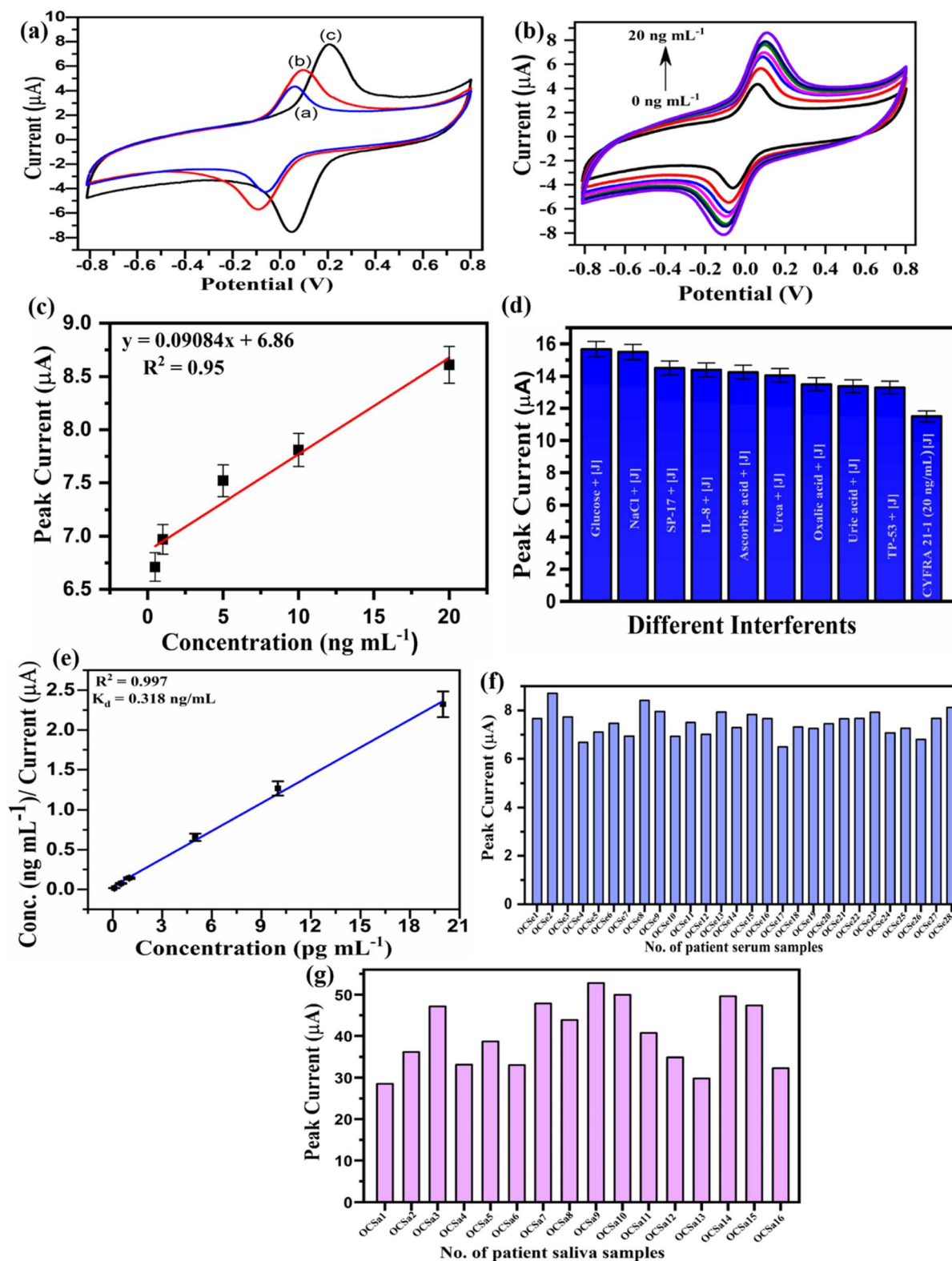
Fig. 4 CYFRA 21-1 biomarker response: (a) comparative study; (b) response study ranging from 0.1 to 20 ng mL^{-1}; (c) calibration plot of the BSA/anti-CYFRA 21-1/SPE bioelectrode between peak current and concentration of CYFRA 21-1; (d) specificity study of the BSA/anti-CYFRA 21-1/SPE bio-electrode; (e) Hanes−Woolf plot, between [CYFRA 21-1 antigen conc.] and [CYFRA 21-1 antigen conc./change in current]; (f) bar plot of cancer patient serum samples depicting current response through the fabricated BSA/anti-CYFRA 21-1/SPE bioelectrode; (g) bar plot of cancer patient saliva samples depicting current response through the fabricated BSA/anti-CYFRA 21-1/SPE bioelectrode.
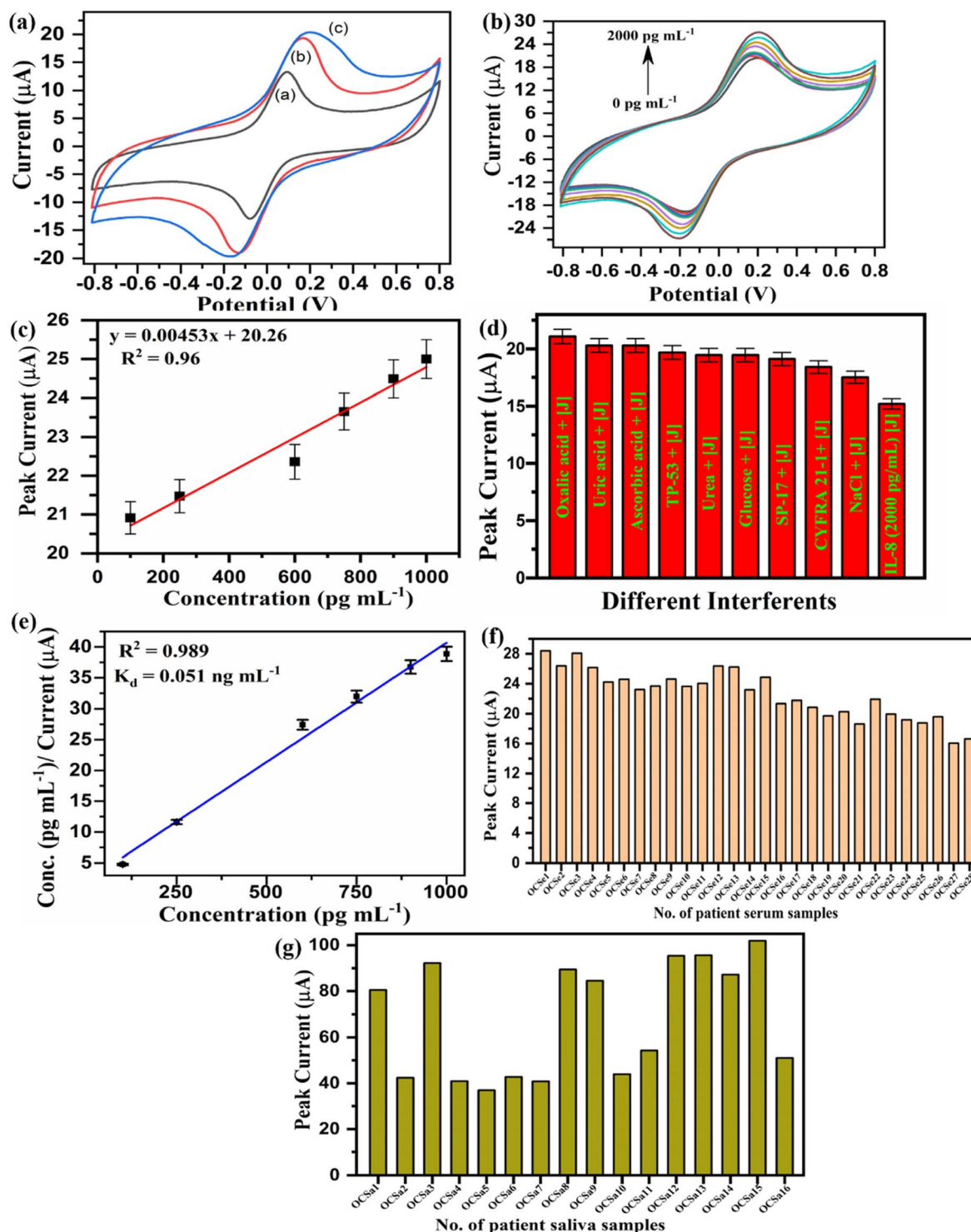
Fig. 5 IL-8 biomarker response: (a) electrode study; (b) response study ranging from 0 to 2000 pg mL^{-1}; (c) calibration plot of the BSA/anti-IL-8/SPE bioelectrode between peak current and concentration of IL-8; (d) specificity study of the BSA/anti-IL-8/SPE bioelectrode; (e) Hanes–Woolf plot, between [IL-8 antigen conc.] and [IL-8 antigen conc./change in current]; (f) bar plot of cancer patient serum samples depicting current response through the fabricated BSA/anti-IL-8/SPE bioelectrode; (g) bar plot of cancer patient saliva samples depicting current response through the fabricated BSA/anti-IL-8/SPE bioelectrode.

addition, Fig. 7(b) and (c) represent the CV of patient serum and saliva samples for the CYFRA 21-1 biomarker-based immunosensor (BSA/anti-CYFRA 21-1/SPE), respectively. These plots represent the change in peak current with respect to the expression level of the biomarker in a particular patient. RSD (%) values were calculated by comparing the current value

Table 2 Estimation of % RSD between peak currents obtained for standard and cancer patient serum samples and determination of CYFRA 21-1 concentration by ELISA using the BSA/anti-CYFRA 21-1/SPE immunoelectrode

S. no.	Patient no.	CYFRA 21-1 (ng mL^{-1}) conc. determined using ELISA	Peak current (μA) obtained from std CYFRA 21-1 samples	Peak current (μA) obtained with patient serum samples	% RSD
1	OCSe 1	1.55	7.63	7.66	0.28
2	OCSe 2	2.71	8.61	8.71	0.82
3	OCSe 3	3.63	7.8	7.73	0.64
4	OCSe 4	0.57	6.62	6.68	0.68
5	OCSe 5	1.72	7.0	7.10	1.00
6	OCSe 6	2.14	7.63	7.46	1.58
7	OCSe 7	2.24	6.97	6.94	0.31
8	OCSe 8	0.46	8.6	8.41	1.50
9	OCSe 9	1.12	7.88	7.95	0.18
10	OCSe 10	0.09	6.97	6.93	0.41
11	OCSe 11	4.51	7.6	7.50	0.94
12	OCSe 12	6.07	6.97	7.01	0.40
13	OCSe 13	0.35	7.88	7.93	0.45
14	OCSe 14	6.53	7.6	7.29	2.85
15	OCSe 15	0.15	7.88	7.83	0.45
16	OCSe 16	4.13	7.63	7.66	0.28
17	OCSe 17	0.84	6.6	6.49	1.19
18	OCSe 18	22.23	7.6	7.31	2.75
19	OCSe 19	1.69	7.6	7.25	2.85
20	OCSe 20	3.16	7.6	7.45	1.3
21	OCSe 21	1.06	7.63	7.65	0.19
22	OCSe 22	0.74	7.63	7.67	0.37
23	OCSe 23	0.84	7.88	7.92	0.36
24	OCSe 24	0.01	6.97	7.07	0.98
25	OCSe 25	3.98	6.97	7.26	2.88
26	OCSe 26	2.6	6.97	6.80	0.92
27	OCSe 27	0.07	7.63	7.67	0.35
28	OCSe 28	0.21	7.9	8.12	1.77

obtained in patient serum samples (Table 2) and saliva samples (Table 3) with that of the standard CYFRA 21-1 antigen sample.

3.5.2. IL-8 biomarker-based immunosensor response. The expression levels of all biomarkers are different; therefore, identical studies were done with IL-8 biomarkers. Fig. 5(a) shows the comparative plot, which exhibited results similar to

the CYFRA 21-1 biomarker that enhanced current after anti-IL-8/SPE and BSA/anti-IL-8/SPE immobilization over the bare SPE.

Fig. 5(b) shows the sensing CV spectrum ranging from 100 pg to 2000 pg mL^{-1}, and Fig. 5(c) shows the calibration plot demonstrating a linearity of 0.96. The calculated LOD and sensitivity for this immunosensor are 0.543 pg mL^{-1} and 0.039 μA mL pg^{-1} cm^{-1}, respectively.

Table 3 Estimation of % RSD among peak currents obtained for standard samples and cancer patient saliva samples, and determination of CYFRA 21-1 concentration by ELISA using the BSA/anti-CYFRA 21-1/SPE immunoelectrode

| S. no.	Patient no.	CYFRA-21-1 conc. (ng mL^{-1}) determined using ELISA	Peak current (μA) obtained from std CYFRA-21-1 samples	Peak current (μA) obtained with patient serum samples	% RSD
1	OCSa 1	52.26	28.93	28.48	1.11
2	OCSa 2	17.14	36.35	36.11	0.47
3	OCSa 3	0.09	47.1	47.11	0.02
4	OCSa 4	42.77	33.13	33.15	0.05
5	OCSa 5	214.15	38.5	38.68	0.33
6	OCSa 6	463.9	33.13	33.05	0.16
7	OCSa 7	52.26	48.1	47.84	0.38
8	OCSa 8	123.7	43.87	43.84	0.05
9	OCSa 9	35.4	52.47	52.79	0.43
10	OCSa 10	53.18	49.25	49.92	0.96
11	OCSa 11	64.27	40.65	40.72	0.12
12	OCSa 12	51.53	34.2	34.86	1.35
13	OCSa 13	59.13	30.97	29.84	2.47
14	OCSa 14	108.8	49.25	49.59	0.49
15	OCSa 15	53.92	47.1	47.36	0.39
16	OCSa 16	82.55	32.05	32.30	0.55
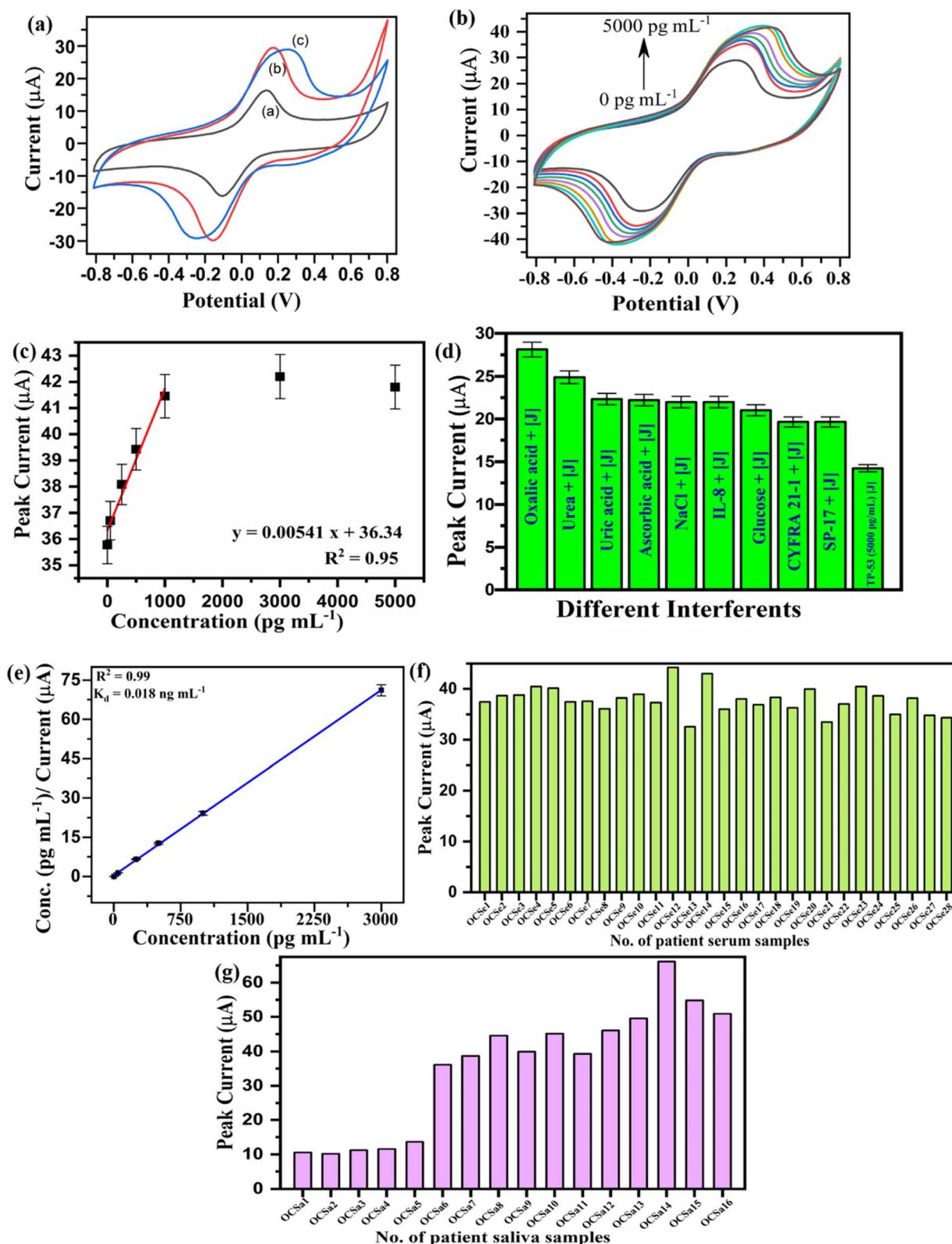
Fig. 6   TP-53 biomarker response: (a) electrode study; (b) response study ranging from 0 to 2000 pg mL^{-1}; (c) calibration plot of the BSA/anti-TP-53/SPE bioelectrode between peak current and concentration of TP-53; (d) specificity study of the BSA/anti-TP-53/SPE bioelectrode; (e) Hanes–Woolf plot, between [TP-53 antigen conc.] and [TP-53 antigen conc./change in current]; (f) bar plot of cancer patient serum samples depicting current response through the fabricated BSA/anti-TP-53/SPE bioelectrode; (g) bar plot of cancer patient saliva samples depicting current response through the fabricated BSA/anti-TP-53/SPE bioelectrode.
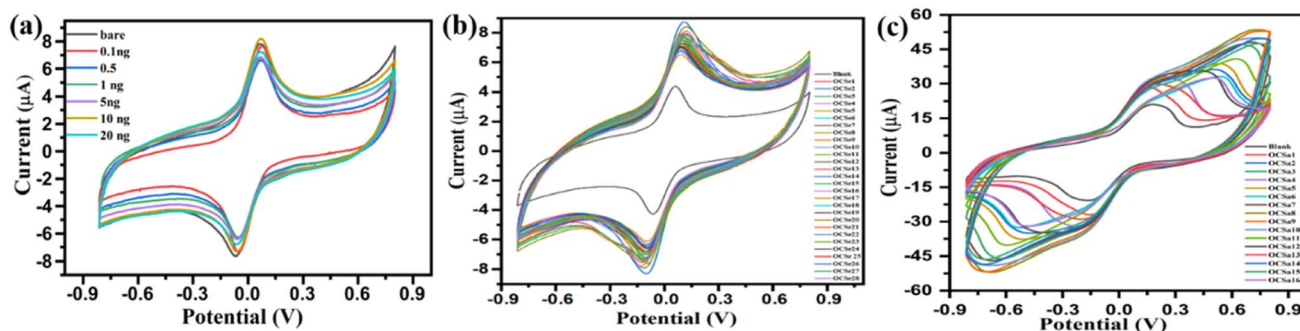
Fig. 7 Cyclic voltammetry studies of the BSA/anti-CYFRA 21-1/SPE immune-electrode: (a) control plot of BSA/anti-CYFRA 21-1/SPE vs. CYFRA 21-1 concentration (0−20 ng mL^{-1}); (b) cancer patient serum sample study using the BSA/anti-CYFRA 21-1/SPE immune-electrode; (c) cancer patient saliva sample study using the BSA/anti-CYFRA 21-1/SPE immune-electrode.
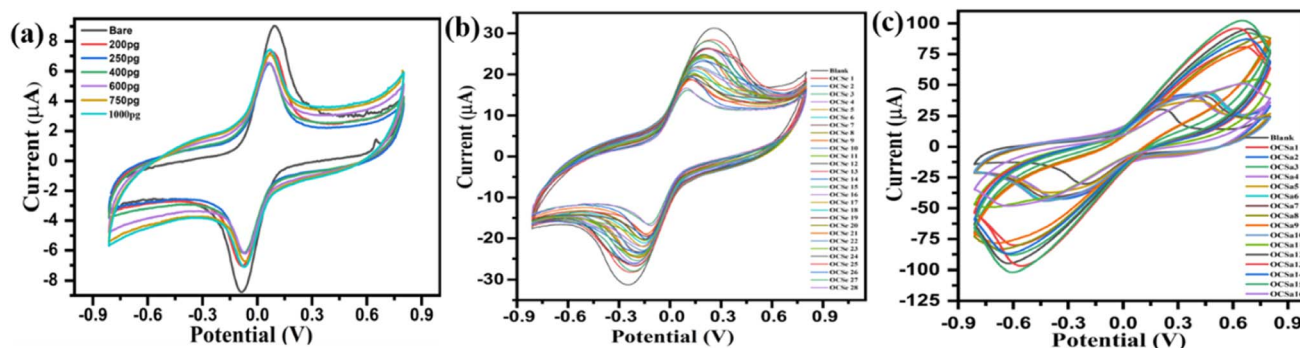

Fig. 8 Cyclic voltammetry studies of the BSA/anti-IL-8/SPE immune-electrode: (a) control plot of BSA/anti-IL-8/SPE vs. IL-8 concentration (0−5000 pg mL^{-1}); (b) cancer patient serum sample study using the BSA/anti-IL-8/SPE immune-electrode; (c) cancer patient saliva sample study using the BSA/anti-IL-8/SPE immune-electrode.

Fig. 5(d) represents the change in anodic peak current upon adding other interfering species in the presence of the IL-8 biomarker to confirm the specificity of the sensor (BSA/anti-IL-8/SPE immunoelectrode). As the immunocomplex was formed between anti-IL-8 and IL-8 antigens, the peak current level decreased drastically compared to other interferents. Interferents such as other biomarkers (SP-17, TP-53, and CYFRA 21-1) and control species were tested. Increased or similar peak current obtained for all species confirms the non-specific interaction with the bound antibody on the electrode surface.

Similarly, the binding affinity between IL-8 and anti-IL-8 on the BSA/anti-IL-8/SPE immunoelectrode surface was analyzed using the Hans–Woolf plot [Fig. 5(e)], with a 0.051 ng mL^{-1} dissociation constant (K_d) value.
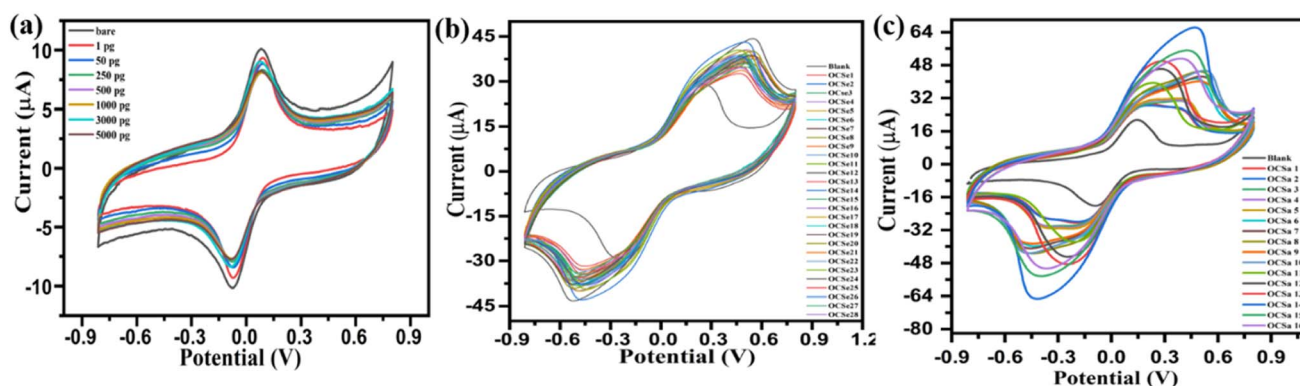

Fig. 9 Cyclic voltammetry studies of the BSA/anti-TP-53/SPE immune-electrode: (a) control plot of BSA/anti-TP-53/SPE vs. TP-53 concentration (0−2000 pg mL^{-1}); (b) cancer patient serum sample study using the BSA/anti-TP-53/SPE immune-electrode; (c) cancer patient saliva sample study using the BSA/anti-TP-53/SPE immune-electrode.
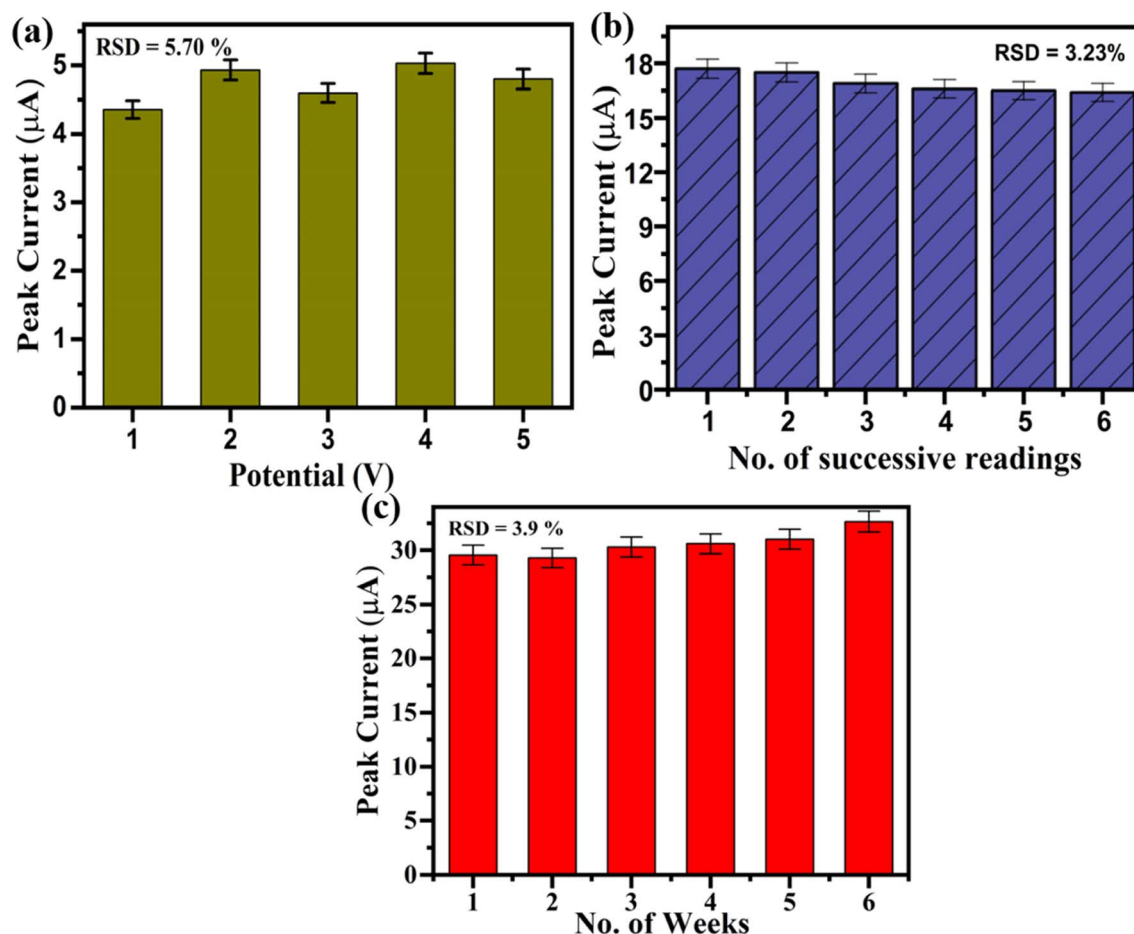
Fig. 10 (a) Reproducibility study for the BSA/anti-CYFRA 21-1/SPE immunoelectrode; (b) repeatability for the BSA/anti-CYFRA 21-1/SPE immunoelectrode; (c) stability for the BSA/anti-CYFRA 21-1/SPE immune-electrode.

Fig. 5(f and g) show the bar graph (peak current *vs.* number of patient serum/saliva samples) of both serum and saliva samples of OC patients for the BSA/anti-IL-8/SPE immunoelectrode, respectively, and their respective values are shown in Tables S2 and S4 in the ESI.† Moreover, Fig. 8(b) and (c) represent the CV of patient serum and saliva samples for the IL-8 biomarker-based immunosensor (BSA/anti-IL-8/SPE), respectively. These plots represent the change in peak current with respect to the expression level of the biomarker in a particular patient. Similarly, RSD (%) values were calculated for serum (Table S2†) and saliva (Table S4†) samples.

3.5.3 TP-53 biomarker-based immunosensor response. Similar studies were conducted to check the expression of TP-53 biomarkers in patients. Fig. 6(a) shows the comparative plot, which exhibited results in the same way as obtained in the case of the CYFRA 21-1 and IL-8 biomarkers.

Fig. 6(b) shows the sensing CV spectrum ranging from 1 pg to 5000 pg mL^{-1}, and Fig. 6(c) shows the calibration plot demonstrating a linearity of 0.95. The calculated LOD and sensitivity for this immunosensor are 1.165 pg mL^{-1} and 0.008 μA mL pg^{-1} cm^{-1}, respectively.

Fig. 6(d) represents the interferent study of the BSA/anti-TP-53/SPE immunoelectrode. The same interferents were employed for testing, and the immunosensor showed the same behavior as in

the case of CYFRA 21-1 and IL-8 biomarkers. BSA/anti-TP-53/SPE immunoelectrode was also tested with other cancer biomarkers such as SP-17, IL-8 and CYFRA 21-1 and immunosensor showed no significant change in peak current.

Similarly, the binding affinity between TP-53 and anti-TP-53 on the BSA/anti-TP-53/SPE immunoelectrode surface was tested using the Hans–Woolf plot [Fig. 6(e)], the attained $K_d = 0.018$ ng mL^{-1}.

Fig. 6(f and g) show the bar graph (peak current *vs.* number of patient serum/saliva samples) of both serum and saliva samples of oral cancer patients for the BSA/anti-TP-53/SPE immune-electrode, respectively, and their respective values are shown in Table S3 and S5 in the ESI.† Likewise, Fig. 9(b) and (c) represent the CV of patient serum and saliva samples for the TP-53 biomarker-based immunosensor (BSA/anti-TP-53/SPE), respectively. These plots represent the change in peak current with respect to the expression level of the biomarker in a particular patient. Likewise, RSD (%) values were calculated for serum samples and saliva samples and given in Table S3 and S5, respectively in the ESI.†

3.6. Control study

3.6.1 For CYFRA-21-1 biomarker-based immunosensor response. Fig. 7(a) represents the control study where a bare
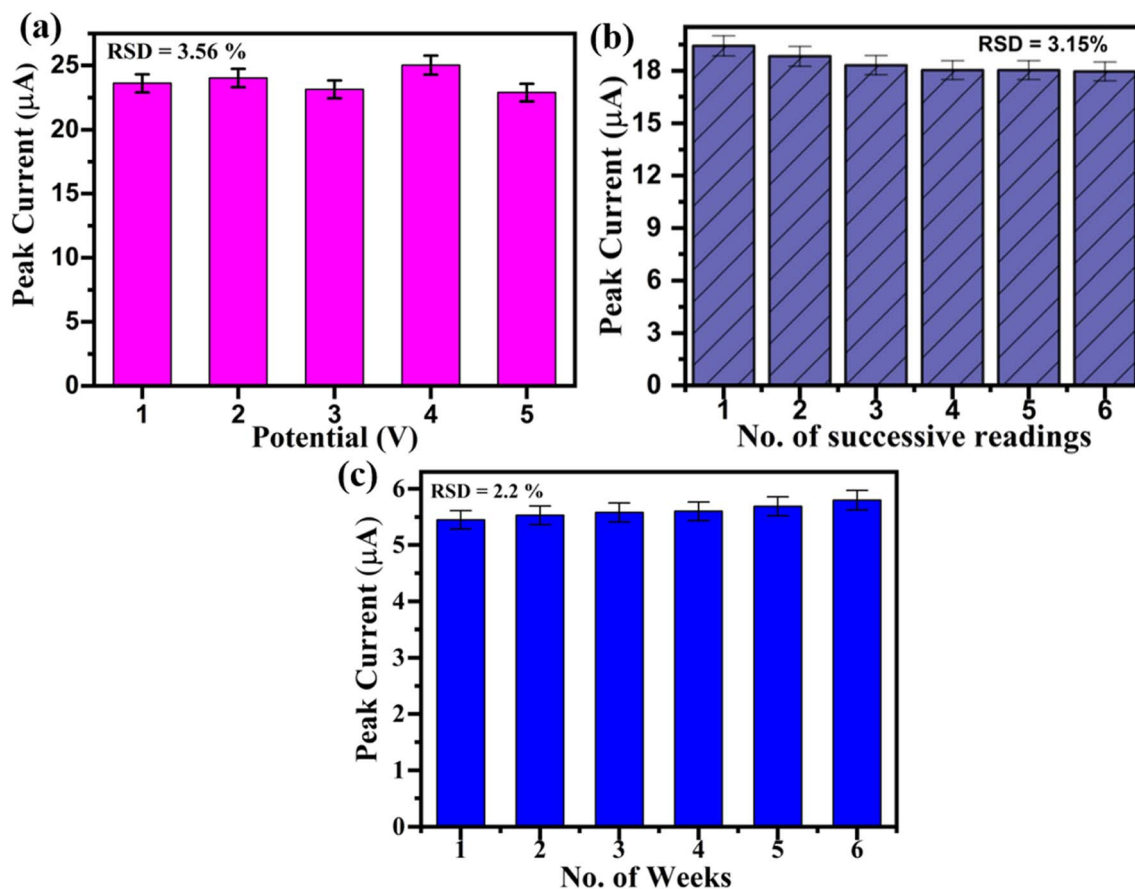
Fig. 11 (a) Reproducibility study for the BSA/anti-IL-8/SPE immunoelectrode; (b) repeatability study for the BSA/anti-IL-8/SPE immunoelectrode; (c) stability study for the BSA/anti-IL-8/SPE immune-electrode.

electrode is exposed to different concentration of the CYFRA 21-1 antigen and no trend in peak current was found with increasing concentration suggesting the fabricated immune electrode to be specific in nature.

3.6.2 For the IL-8 biomarker-based immunosensor. Fig. 8(a) represents the control study where a bare electrode is exposed to different concentrations of IL-8 antigen and no trend in peak current was found with increasing concentration suggesting the fabricated immune electrode to be specific in nature.

3.6.3 For the TP-53 biomarker-based immunosensor. Fig. 9(a) represents the control study where a bare electrode is exposed to different concentrations of TP-53 antigen and no trend in peak current was found with increasing concentration suggesting the fabricated immune electrode to be specific in nature.

3.7. Reproducibility, repeatability, and stability studies

3.7.1 For the CYFRA-21-1 immunoelectrode. Fig. 10(a) shows the reproducibility plot of BSA/anti-CYFRA 21-1/SPE using the CV technique for five different electrodes. The bar plot indicates 5.70% relative standard deviation (RSD), which shows high reproducibility. Fig. 10(b) represents the bar plot of the repeatability study for BSA/anti-CYFRA 21-1/SPE for

five different consecutive readings, which were measured with a 3.23% RSD value. This value indicated the high repeatable nature of the electrode. Fig. 10(c) shows the stability plot of the BSA/anti-CYFRA 21-1/SPE immune-electrode and its storage ability was determined by acquiring CV readings for regular intervals of one week up to 6 weeks, demonstrating 3.9% RSD.

3.7.2 For IL-8 immunoelectrode. Fig. 11(a) shows the reproducibility plot of BSA/anti-IL-8/SPE using the CV technique for five different electrodes. The bar plot indicates 3.56% relative standard deviation (RSD), which shows high reproducibility. Fig. 11(b) represents the bar plot of the repeatability study for BSA/anti-IL-8/SPE for five different consecutive readings, which were measured with a 3.15% RSD value. This value indicated the high repeatable nature of the electrode. Fig. 11(c) shows the stability plot of the BSA/anti-IL-8/SPE immune-electrode and its storage ability was determined by acquiring CV readings for regular intervals of one week up to 6 weeks, demonstrating 2.2% RSD.

3.7.3 For the TP-53 immunoelectrode. Fig. 12(a) shows the reproducibility plot of BSA/anti-TP-53/SPE using the CV technique for five different electrodes. The bar plot indicates 3.25% relative standard deviation (RSD), which shows high reproducibility. Fig. 12(b) represents the bar plot of the repeatability study for BSA/anti-TP-53/SPE for five different
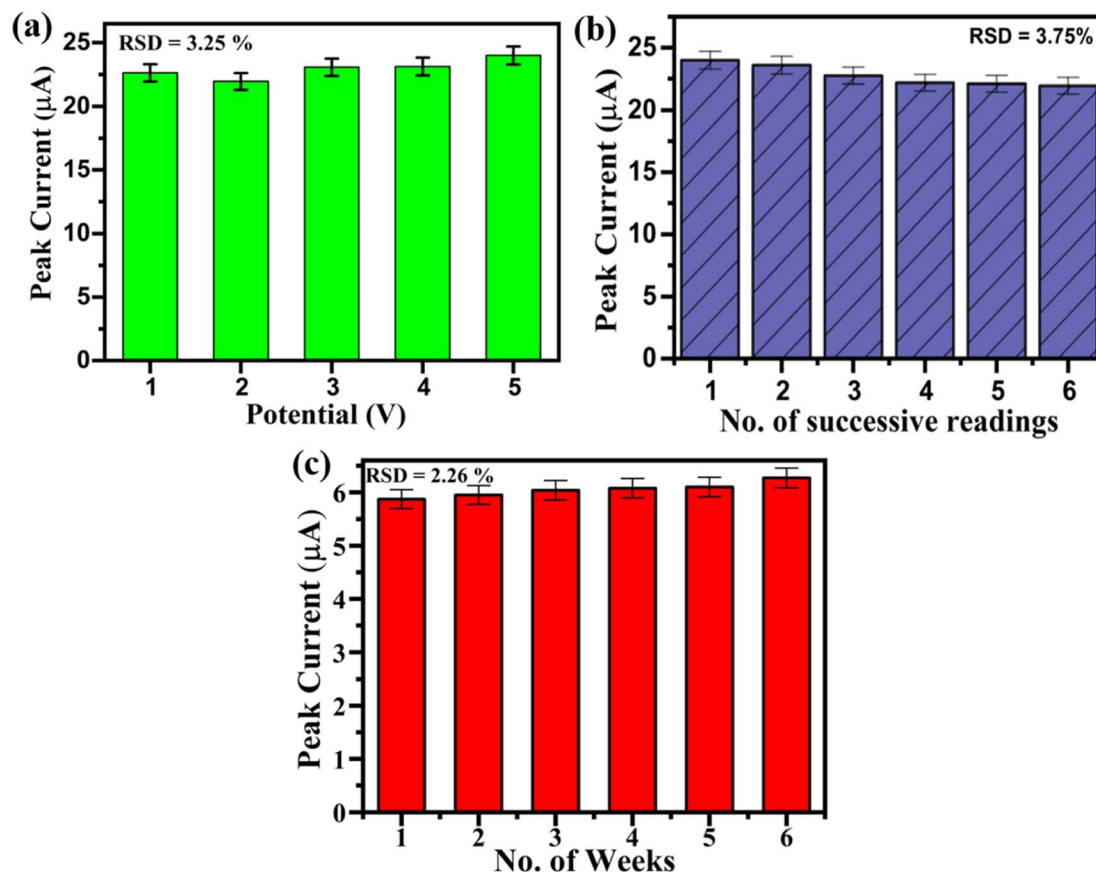
Fig. 12 (a) Reproducibility study for the BSA/anti-TP-53/SPE immunoelectrode; (b) repeatability study for the BSA/anti-TP-53/SPE immunoe-lectrode; (c) stability study for the BSA/anti-TP-53/SPE immune-electrode.
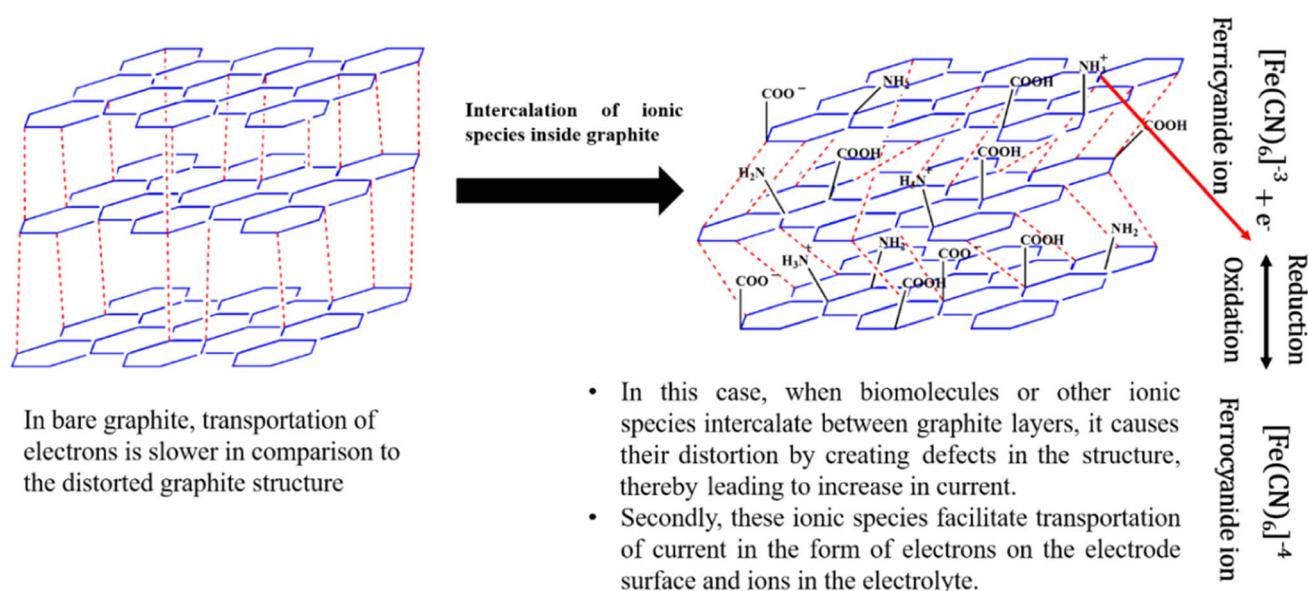

Fig. 13 Mechanism of charge transfer from the graphite-based SPE and after the immobilization of biomolecules or interferents.

consecutive readings, which were measured with a 3.75% RSD value. This value indicated the high repeatable nature of the electrode. Fig. 12(c) shows the stability plot of the BSA/anti-TP-53/SPE immunoelectrode and its storage ability was determined by acquiring CV readings for regular intervals of one week up to of 6 weeks, demonstrating 2.26% RSD.

For all the fabricated immunosensors, it was observed that the current was found stable up to 5 weeks and thereafter, it started rising in every immunosensor due to the degradation of biomolecules which unfold and intercalate between 2D graphene layers promoting realignment of layers, thus causing more defects in the graphite structure, which promote increase in current.[46,47]

4. Mechanism of charge transfer

The graphite structure comprises two geometries: hexagonal (ABAB) and rhombohedral (ABCABC). Rhombohedral is <30% due to thermodynamical instability. Therefore, the graphite structure acquires structural changes upon the intercalation of ions or molecules (called intercalants). According to Rudorff, 'n' is the number of graphene layers that separate two intercalate layers. As a result, when intercalants within the graphite host structure increase, the number of empty layers correspondingly, i.e., '$n - 1$', decreases. The graphene layers of graphite make flexible islands that allow intercalants to slide or diffuse within the layers, thus forming a lower or higher stage upon intercalation and changing the symmetry of the structure, thereby promoting the restacking of graphene layers. Intercalants responsible for restacking include Abs, BSAs, and Ags, and other control species get incorporated into the islands. Intercalants are responsible for restacking of layers and, thus, increasing current upon voltage variation.

5. Conclusion

Remarkably sensitive and indigenous test strips were developed in the laboratory to detect OC early in the patient's serum and saliva samples. Laboratory-made SPEs offer several advantages over other reported electrodes. The advantages are that they do not require nanomaterial functionalization for covalent immobilization of biomolecules and are flexible, conductive, disposable, miniaturized, and cost-effective, and work in a broader sensing range. In this manuscript three different immunosensors were fabricated to detect OC biomarkers CYFRA 21-1, IL-8, and TP-53 based on different immunosensing platforms, including anti-CYFRA 21-1, anti-IL-8, and anti-TP-53, respectively, on the SPEs. These immunosensors demonstrated significantly lower detection limits of 829.5 pg mL^{-1}, 0.543 pg mL^{-1}, and 1.165 pg mL^{-1}, and excellent sensitivity of 0.935 μA mL pg^{-1} cm^{-1}, 0.039 μA mL pg^{-1} cm^{-1}, and 0.008 μA mL pg^{-1} cm^{-1} for CYFRA 21-1, IL-8, and TP-53 biomarkers, respectively. With the help of these fabricated immunosensors, capable of detecting oral biomarkers such as CYFRA 21-1, IL-8, and TP-53, it is easy to detect OC accurately and rapidly. This study represents the fabricated immunosensors' efficiency in detecting OC in the patient's serum and saliva samples. Saliva samples showed more biomarker concentration than serum samples, as saliva is in direct contact with cancer lesions. The concentration of OC biomarkers such as CYFRA 21-1, IL-8, and TP-53 was determined from the conventional detection method ELISA. SPE-based immunosensors demonstrated excellent sensitivity, specificity, a lower detection limit, stability, reproducibility, and repeatability. These test strips can be taken further for device fabrication. Moreover, the sensing with all three biomarkers was performed in the physiological range and cancerous range of all the biomarkers. The purpose of working with all three biomarkers is to find out the expression level of all three biomarkers in different patients and to detect OC.

Conflicts of interest

There are no conflicts to declare.

References

1 A. Gorschinski, G. Khelashvili, D. Schild, W. Habicht, R. Brand, M. Ghafari, H. Bönnemann, E. Dinjus and S. Behrens, *J. Mater. Chem.*, 2009, **19**, 8829–8838.
2 C. Laprise, H. P. Shahul, S. A. Madathil, A. S. Thekkepurakkal, G. Castonguay, I. Varghese, S. Shiraz, P. Allison, N. F. Schlecht and M. Rousseau, *Int. J. Cancer*, 2016, **139**, 1512–1519.
3 R. Mehrotra and D. K. Gupta, *Head Neck Oncol.*, 2011, **3**, 1–9.
4 A. K. Yadav, D. Verma and P. R. Solanki, *ACS Appl. Bio Mater.*, 2023, 4250–4268.
5 C. A. Righini, F. de Fraipont, J.-F. Timsit, C. Faure, E. Brambilla, E. Reyt and M.-C. Favrot, *Clin. Cancer Res.*, 2007, **13**, 1179–1185.
6 D. Sidransky, *Science*, 1997, **278**, 1054–1058.
7 M. S. Fliss, H. Usadel, O. L. Caballero, L. Wu, M. R. Buta, S. M. Eleff, J. Jen and D. Sidransky, *Science*, 2000, **287**, 2017–2019.
8 S. S. Sawant, S. M. Zingde and M. M. Vaidya, *Oral Oncol.*, 2008, **44**, 722–732.
9 A. Katakura, I. Kamiyama, N. Takano, T. Shibahara, T. Muramatsu, K. Ishihara, R. Takagi and T. Shouno, *Bull. Tokyo Dent. Coll.*, 2007, **48**, 199–203.
10 S. Duffy, J. Taylor, J. Terrell, M. Islam, Z. Yuan, K. Fowler, G. Wolf and T. Teknos, *Cancer Res.*, 2007, **67**(9_Supplement), 3412.
11 N. L. Rhodus, V. Ho, C. S. Miller, S. Myers and F. Ondrey, *Cancer Detect. Prev.*, 2005, **29**, 42–45.
12 L. P. Zhong, G. F. Chen, Z. F. Xu, X. Zhang, F. Y. Ping and S.-F. Zhao, *Int. J. Oral Maxillofac. Surg.*, 2005, **34**, 566–570.
13 P. H. Liao, Y. C. Chang, M. F. Huang, K. W. Tai and M. Y. Chou, *Oral Oncol.*, 2000, **36**, 272–276.
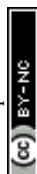
14 M. J. Fackler, M. McVeigh, J. Mehrotra, M. A. Blum, J. Lange, A. Lapides, E. Garrett, P. Argani and S. Sukumar, *Cancer Res.*, 2004, **64**, 4442–4452.

15 Y. Wan, W. Deng, Y. Su, X. Zhu, C. Peng, H. Hu, H. Peng, S. Song and C. Fan, *Biosens. Bioelectron.*, 2011, **30**, 93–99.

16 S. Verma, A. Singh, A. Shukla, J. Kaswan, K. Arora, J. Ramirez-Vick, P. Singh and S. P. Singh, *ACS Appl. Mater. Interfaces*, 2017, **9**, 27462–27474.

17 S. Verma and S. P. Singh, *MRS Commun.*, 2019, **9**, 1227–1234.

18 R. Sharma, S. E. Deacon, D. Nowak, S. E. George, M. P. Szymonik, A. A. S. Tang, D. C. Tomlinson, A. G. Davies, M. J. McPherson and C. Wälti, *Biosens. Bioelectron.*, 2016, **80**, 607–613.

19 S. Tiwari, P. K. Gupta, Y. Bagbi, T. Sarkar and P. R. Solanki, *Biosens. Bioelectron.*, 2017, **89**, 1042–1052.

20 H. Wang, X. Gao and Z. Ma, *Sci. Rep.*, 2017, **7**, 1–7.

21 N. Pachauri, K. Dave, A. Dinda and P. R. Solanki, *J. Mater. Chem. B*, 2018, **6**, 3000–3012.

22 P. K. Wilson, T. Jiang, M. E. Minunni, A. P. F. Turner and M. Mascini, *Biosens. Bioelectron.*, 2005, **20**, 2310–2313.

23 A. K. Yadav, P. Gulati, R. Sharma, A. Thakkar and P. R. Solanki, *Talanta*, 2022, 123376.

24 A. K. Yadav, D. Verma, A. Kumar, A. N. Bhatt and P. R. Solanki, *Int. J. Biol. Macromol.*, 2023, 124325.

25 A. K. Yadav, D. Verma, A. Kumar, P. Kumar and P. R. Solanki, *Mater. Today Chem.*, 2021, 100443.

26 D. Verma, K. R. B. Singh, A. K. Yadav, V. Nayak, J. Singh, P. R. Solanki and R. P. Singh, *Biosens. Bioelectron.: X*, 2022, **11**, 100153.

27 S. N. Banitaba, S. Khademolqorani, V. V Jadhav, E. Chamanehpour, Y. K. Mishra, E. Mostafavi and A. Kaushik, *Mater. Today Electron.*, 2023, **5**, 100055.

28 M. Byakodi, N. S. Shrikrishna, R. Sharma, S. Bhansali, Y. Mishra, A. Kaushik and S. Gandhi, *Biosens. Bioelectron.: X*, 2022, **12**, 100284.

29 C. Grisales, N. Herrera and F. Fajardo, *Phys. Educ.*, 2016, **51**, 055011.

30 A. K. Yadav, D. Verma, G. B. V. S. Lakshmi, S. Eremin and P. R. Solanki, *Food Chem.*, 2021, **363**, 130245.

31 N. G. Welch, J. A. Scoble, B. W. Muir and P. J. Pigram, *Biointerphases*, 2017, **12**, 02D301.

32 A. K. Yadav, D. Verma and P. R. Solanki, *Mater. Today Chem.*, 2021, **22**, 100567.

33 A. Nurkka, J. Obiero, H. Kayhty and J. A. G. Scott, *Clin. Vaccine Immunol.*, 2003, **10**, 357–361.

34 R. L. Hodinka, T. Nagashunmugam and D. Malamud, *Clin. Diagn. Lab. Immunol.*, 1998, **5**, 419–426.

35 I. O. Faniyi, O. Fasakin, B. Olofinjana, A. S. Adekunle, T. V Oluwasusi, M. A. Eleruja and E. O. B. Ajayi, *SN Appl. Sci.*, 2019, **1**, 1–7.

36 C. A. Ibekwe, G. M. Oyatogun, T. A. Esan and K. M. Oluwasegun, *Am. J. Mater. Sci. Eng.*, 2017, **5**(1), 28–36.

37 A. K. Yadav, T. K. Dhiman, G. Lakshmi, A. N. Berlina and P. R. Solanki, *Int. J. Biol. Macromol.*, 2020, **151**, 566–575.

38 D. Chauhan, A. K. Yadav and P. R. Solanki, *Microchim. Acta*, 2021, **188**, 1–11.

39 D. Verma, D. Chauhan, M. Das Mukherjee, K. R. Ranjan, A. K. Yadav and P. R. Solanki, *J. Appl. Electrochem.*, 2021, **51**, 447–462.

40 D. Verma, A. K. Yadav, M. Das Mukherjee and P. R. Solanki, *J. Environ. Chem. Eng.*, 2021, **9**, 105504.

41 Y. H. Chung, T. Lee, S.-Y. Yoo, J. Min and J.-W. Choi, *Sci. Rep.*, 2015, **5**, 1–9.

42 D. D. L. Chung, *J. Mater. Sci.*, 2002, **37**, 1475–1489.

43 T. Tran and K. Kinoshita, *J. Electroanal. Chem.*, 1995, **386**, 221–224.

44 M. Baccarin, S. J. Rowley-Neale, É. T. G. Cavalheiro, G. C. Smith and C. E. Banks, *Microchim. Acta*, 2019, **186**, 1–9.

45 G. Aydoğdu, D. K. Zeybek, Ş. Pekyardımcı and E. Kılıç, *Artif. Cells, Nanomed., Biotechnol.*, 2013, **41**, 332–338.

46 L. J. Lapidus, *F1000Research*, 2017, 6.

47 J. Asenbauer, T. Eisenmann, M. Kuenzel, A. Kazzazi, Z. Chen and D. Bresser, *Sustainable Energy Fuels*, 2020, **4**, 5387–5416.

48 N. Elgrishi, K. J. Rountree, B. D. McCarthy, E. S. Rountree, T. T. Eisenhart and J. L. Dempsey, *J. Chem. Educ.*, 2018, **95**, 197–206.